Collagen and Leather

RESEARCH

Open Access

Xylan derived carbon sphere/graphene composite film with low resistance for supercapacitor electrode

Jihai Cai[1], Yujin Li[2], Rongji Qin[3], Guangsheng Li[1] and Xiaoying Wang[1]*

Abstract

Reduced graphene oxide (rGO) films suffer from low capacitance for inner unreduced oxygen functional groups, restacking of sheets and high contact resistance. Herein, carbon spheres derived from renewable xylan were added to graphene oxide with large sheet area to fabricate film by gelation and filtration, followed by in situ reduction for high-performance flexible supercapacitor. rGO film with transverse size about 13 μm showed a good specific capacitance of 967 mF/cm^2 at a scanning rate of 5 mV/s and increased to 1786 mF/cm^2 by in situ reducing its inner part, which generally remained oxidized due to outer hindering from hydrophobic graphene. Then, by hydrothermal carbonization of xylan and activation with KOH, activated carbon sphere (aXCS) was prepared, which had a diameter of 150–200 nm and a specific capacitance of 270 F/g. The aXCS acted as spacer and connector to avoid restacking of graphene sheets and decrease interlayer contact resistance, resulting 94% increase in capacitance performance from rGO film to aXCS/rGO film. Therefore, combined in situ reduction and enhancement through compositing aXCS, the final film (aXCS/rGO-AA) showed a boosted specific capacitance of 755 mF/cm^2 at 1 mA/cm^2 in double electrode system, power density of 22.5–2250 mW/cm^2, and energy density of 11.88–25.2 mWh/cm^2. Meanwhile, aXCS/rGO-AA had outstanding cycling stability that its specific capacitance maintained 108.7% after 10,000 cycles of charge–discharge, showing promising potential in wearable and portable electronics.

Keywords Xylan, Carbon sphere, Graphene film, In situ reduction, Supercapacitor
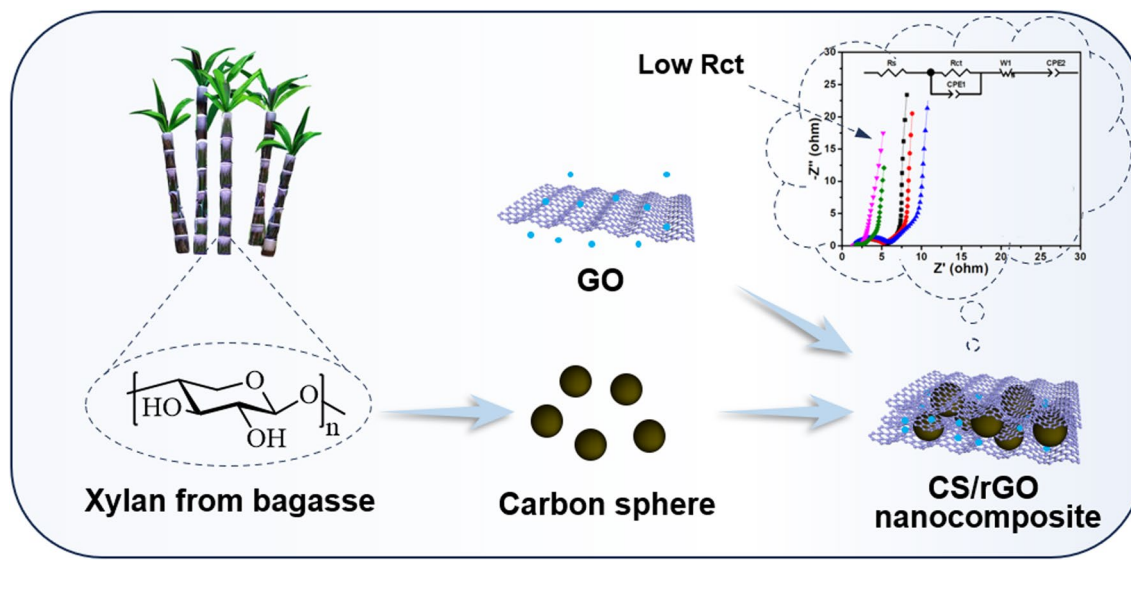
*Correspondence:
Xiaoying Wang
xyw@scut.edu.cn
Full list of author information is available at the end of the article

Springer Open

Cai *et al. Collagen and Leather*   (2024) 6:9

Page 2 of 14

Graphical abstract

1 Introduction

Supercapacitor is an efficient and green energy storage device with characteristics of fast charging/discharging speed, long cycle life, environment friendliness, and high safety [1–3]. Due to high conductivity, special thermal conductivity, mechanical properties and large specific surface area, graphene is widely utilized as electrode component for electrical double-layer capacitor [4, 5]. Large-scale fabrication of graphene is generally through chemical conversion of graphite to graphene oxide (GO) and followed reduction [6]. Hydrophilic functional groups of GO enable modification and handling by dispersing in aqueous solution, which can be assembled into an ordered structure to fabricate super strong film through directional flow [7]. However, it still remains as a challenge to improve capacitance of graphene film for partly reducing of graphene oxide, restacking of graphene sheets and high interlayer contact resistance.

Fabricating GO with large sheets area by relative mild oxidation of H_2SO_4 and $KMnO_4$ is an efficient way to cut down contact resistance between graphene sheets. In following reduction, although thermal annealing shows amazing enhancement on conductivity of GO film, its mechanical properties are greatly deteriorated with terrible restacking of sheets at same time, which hinders capacitor performance [8]. Chemical reduction by reagents without generation of gas negligibly act on restacking and mechanical failure [9, 10]. However, transformation of hydrophilic GO to hydrophobic rGO on the surface blocks permeation of reducing agent to inner part. These oxygen functional groups lower rate of electronic transfer and rate performance. Hence, if the GO could be in situ reduced, its performance as electrode for flexible supercapacitor would be enhanced. GO film prepared by filtration before drying still contains small amount of solution, which may load ascorbic acid for in situ induction. Its loading capacity would increase by gelation of GO that the cross-linked network reserved more solution. Meanwhile, it usually takes long time for GO solution to filtrate into a film for hydrophilicity and small size of GO. Gelation of GO by protonation and van der Waals interaction will accelerate velocity of filtration.

However, after in situ reduction of GO composite film, there are ascorbic acid and its oxidation products residual in interlayer space between graphene sheets. Their poor conductivity leads to high interlayer contact resistance. Carbon sphere is a kind of materials with low voltage drop, preparing by hydrothermal reaction of carbohydrates [11, 12]. Exploiting carbon spheres as spacers for graphene will effectively improve interlayer charge transfer speed, reduce aggregation of graphene, and improve capacitance performance. Graphene layers also play a role in supporting and fixing carbon spheres in turn [13]. In various precursors for preparation of carbon sphere, xylan is renewable, highly available, environmentally friendly, which is the main type of hemicellulose in hardwood and Gramineae plants [14, 15]. Conversion to carbon sphere provides a way for utilization of xylan which churns out annually as agricultural and forestry wastes. Furthermore, compared with other carbohydrates, xylan

generated carbon in a higher yield [16]. During process of hydrothermal carbonization of xylan, a large amount of pentose is generated through hydrolysis, which forms furfural through dehydration and subsequently form carbon spheres. Up to now, there is few research reported the preparation of carbon spheres with xylan as raw material.

Therefore, in this paper, xylan was dissolved in NaOH/urea to prepare carbon sphere through hydrothermal reaction, which was then activated by KOH. Carbon spheres/graphene composite film was prepared by sequential gelation, filtration and reduction of solution mixed with ascorbic acid, graphite oxide and activated carbon spheres. It was found that activated carbon sphere (aXCS) was evenly dispersed between sheets of rGO and GO was in situ reduced by ascorbic acid in the composite film. Charge transfer resistance was diminished and stacking of graphene sheets was avoided in this way.

2 Materials and methods

2.1 Chemical and materials
Xylan (extracted from bagasse) and cellulose ester dialysis membranes (100–500 Da) were provided by Shanghai Yuanye Bio-technology Co., Ltd (Shanghai, China). Flake graphite (325 mesh) was supplied by XF Nano Co., Ltd (Nanjing, China). All other chemicals were of analytical grade. A ELF11/6B/301 maffle furnace was obtained from Verder Shanghai Instrument Equipment Co., Ltd (Shanghai, China). An OTF-1200X-S tubular furnace with maximum heating temperature of 1200 °C was purchased from Hefei Kejing Material Technology Co., Ltd (Hefei, China). CHI660E electrochemical workstation was supplied by Shanghai Chenhua Instrument Co., Ltd (Shanghai, China).

2.2 Preparation of graphene oxide
Preparation of GO was based on a reported method with minor modification [17]. 24 mL of concentrated sulfuric acid was cooled to 0 °C, then, 0.5 g of graphite and 0.5 g of $NaNO_3$ were added under stirring, respectively. In ice water bath, 3 g of $KMnO_4$ was slowly added to the mixture and stirred at 100 rpm for 90 min. Then, the mixture was heated to 35 °C and reacted for 2 h. Subsequently, 20 mL of deionized water was added to the mixture by a LSP02-2A syringe pump in 30 min. After reaction, 50 mL of deionized water was used to dilute the mixture and 2.5 mL of 30% H_2O_2 was added to remove excess $KMnO_4$. The obtained pale brown graphite oxide suspension was washed by repeated centrifugation with 10% HCl and deionized water. And graphite oxide sediment was dispersed in 1000 mL of deionized water. Then, GO was obtained by mild sonication to exfoliate graphite oxide. By low-speed centrifugation (3000 rpm, 5 min),

multilayered GO was removed and the pH was adjusted to about 10 by 10 mL of ammonia.

2.3 Preparation of rGO-AA composite film
Ascorbic acid was completely dissolved in GO solution by stirring and the mixture was filtrated after adding HCl to prepare GO-AA composite film, which was dried at 45 °C for 12 h. Then, the GO-AA composite film was immersed in 40 mL of 3% ascorbic acid solution and heated to 90 °C for 30 min. After drying, rGO-AA-1~4 composite films were obtained by varying concentration of ascorbic acid (7.78, 15.56, 23.34 and 38.9 mg/mL) added to GO solution.

2.4 Preparation of xylan derived carbon sphere (XCS)
Firstly, 10 g of NaOH and 15 g of urea was dissolved in 100 mL of deionized water to prepare NaOH/urea solution (7 wt% NaOH and 12 wt% urea). Then, xylan powder was added to 20 mL of NaOH/urea solution, followed by stirring until xylan was completely dissolved. The obtained xylan solution was poured in stainless steel autoclave with Teflon lining and put in muffle furnace for hydrothermal reaction. After reaction, the mixture was centrifuged at 14,000 rpm for 10 min and precipitate was repeatedly centrifuged with deionized water until pH of supernatant is neutral. Xylan carbon sphere was obtained by vacuum drying overnight at 45 °C. As shown in Table 1, by changing solvent, concentration of xylan and reaction time, various XCSs were prepared (XCS-1~6).

2.5 Activation of XCS
XCS was immersed in KOH solution and was evenly dispersed by ultrasound at 240 W for 30 min. After standing for 24 h, the mixture was centrifuged at 14,000 rpm for 10 min to remove supernatant, followed by drying in vacuum drying oven at 45 °C for 12 h. Obtained powder was ground and put in tubular furnace. With high-purity nitrogen, the tubular furnace was heated to 350 °C at heating rate of 2 °C/min and kept for 1 h. Then, it was heated to 800 °C at heating rate of 5 °C/min and kept for 1 h. After natural cooling, black powder was obtained,

Table 1 Preparation of XCS in various conditions

Sample	Solvent	Concentration (g/mL)	Temperature (°C)	Time (h)
XCS-1	2% NaOH	0.05	240	12
XCS-2	NaOH/urea	0.05	240	12
XCS-3	NaOH/urea	0.005	240	24
XCS-4	NaOH/urea	0.025	240	24
XCS-5	NaOH/urea	0.05	240	24
XCS-6	NaOH/urea	0.1	240	24

Table 2 Preparation of porous xylan carbon sphere in various conditions

Sample	Concentration of KOH (mol/L)	Temperature (°C)	Time (h)	Capacitor (F/g)
aXCS-1	0.2	700	1	80
aXCS-2	0.2	800	1	270
aXCS-3	0.2	900	1	112
aXCS-4	0.05	800	1	52
aXCS-5	0.1	800	1	98
aXCS-6	1.5	800	1	150
aXCS-7	2.5	800	1	178
aXCS-8	0.2	800	0.5	108
aXCS-9	0.2	800	2	60

which was washed by 10% HCl and dried subsequently. As shown in Table 2, via changing the concentration of KOH, temperature, and time, various active XCSs were prepared (aXCS-1~9).

2.6 Preparation of aXCS/rGO composite film

aXCS was dispersed in 5 mL of deionized water by sonication, which was added dropwise to GO solution. aXCS/GO composite film was obtained by filtration after addition of HCl to induce gelation of GO and dried at 45 °C for 12 h. 1.2 g of ascorbic acid was dissolved in 40 mL of deionized water, and aXCS/GO composite film was immersed in the solution and reacted at 90 °C to obtain aXCS/rGO. By varying the dosage of aXCS (5%, 10%, 20% and 40%), $aXCS_{0.05}$/rGO, $aXCS_{0.1}$/rGO, $aXCS_{0.2}$/rGO, and $aXCS_{0.4}$/rGO were prepared, respectively.

2.7 Preparation of aXCS/rGO-AA composite film

Ascorbic acid was completely dissolved in GO solution by stirring. The concentration of ascorbic acid in the mixture was 23.34 mg/mL. Then, aXCS was dispersed in water by sonication, followed by adding dropwise to GO-ascorbic acid. aXCS/GO-AA composite film was obtained by filtration after adding HCl and drying at 45 °C for 12 h. The composite film was reduced by 3% ascorbic acid solution at 90 °C for 30 min and dried to prepared aXCS/GO-AA composite film.

2.8 Characterization

The micromorphology of GO was detected by atomic force microscopy (AFM) (Veeco Nanoscope III, America) in air under ambient conditions in tapping mode. Images of GO and films were investigated by Scanning electron microscope (SEM) (Zeiss Merlin, Germany).

2.9 Electrochemical performance

Electrochemical performance of aXCS/GO-AA composite film was investigated on a CHI660E electrochemical work station. In three-electrode system, calomel electrode, platinum sheet electrode, composite film and 6 M KOH were reference electrode, counter electrode, working electrode and electrolyte, respectively. Cyclic voltammetry (CV) curve, galvanostatic charge/discharge (GCD) curve, and cyclic stability were tested in voltage window of − 1 to − 0.1 V. Nyquist curve was measured in frequency range of 10–0.1 MHz and at amplitude of 5 mV. Capacitor of aXCS was measured by similar method. 4 mg of aXCS was dispersed in 1 mL ethanol/water (1/4, v/v) solution with 8 μL of nafion as binder. After sonication at 320 W for 15 min, 5 μL of the mixture was dripped on glassy carbon electrode, followed by drying in oven. With the glassy carbon electrode as working electrode, electrochemical performance of aXCS was tested.

In three-electrode system, mass specific capacitance of electrode at various scan rate was calculated by following equation based on CV [18]:

$$C_s = \frac{\int \mathrm{IdV}}{vm\Delta V} \tag{1}$$

where Cs was mass specific capacitance (F/g), I was response current (A), v was scan rate (V s^{-1}), m was mass of active material on working electrode (g), ΔV was voltage window (V).

Areal specific capacitor of working electrode at various scan rates was calculated by the following equation:

$$C_A = \frac{\int \mathrm{IdV}}{vS\Delta V} \tag{2}$$

where C_A was areal specific capacitor (mF/cm^2), I was response current (mA), v was scan rate (V s^{-1}), ΔV was voltage window (V), S was area of working electrode (cm^2).

Based on GCD, areal capacitor of working electrode at various current density was calculated by following equation:

$$C_A = \frac{I\Delta t}{S\Delta V} \tag{3}$$

where I was charging current (A/cm^2), Δt was charging time in one cycle (s), S was area of working electrode (cm^2), ΔV was voltage drop during discharge (IR drop at beginning of discharge is not included).

In two-electrode system, working electrode and counter electrode were composite film with the same area and areal capacitor was calculated by following equation:

Cai *et al. Collagen and Leather*   (2024) 6:9

Page 5 of 14

$$C_A = \frac{4I\Delta t}{S\Delta V} \tag{4}$$

where I was discharging current (A/cm^2), Δt was discharging time (s), S was area of working electrode and counter electrode (cm^2), ΔV was voltage drop during discharge (the IR drop at the beginning of discharge is not included).

The energy density of two-electrode system was calculated by following equation:

$$E = \frac{C_A \Delta V^2}{4 \times 2 \times 3.6} \tag{5}$$

where E was energy density of two-electrode system (Wh/cm^2), ΔV was voltage drop during discharge (the IR drop at the beginning of discharge is not included).

Power density of the two-electrode system was calculated by following equation [19]:

$$P = \frac{3600E}{\Delta t} \tag{6}$$

where P was power density of two-electrode system (mW/cm^2), Δt was discharging time (s).

3 Results and discussion

3.1 Electrochemical performance of rGO-AA film

In order to improve performance of rGO film (Additional file 1: Fig. S1 and S2), ascorbic acid was added to GO solution before filtration. The film obtained by filtration still retained part of water before drying, which contained ascorbic acid. In subsequent reduction, ascorbic acid retained in the GO film could in situ reduce its internal part, avoiding the difficulty of ascorbic acid to penetrate interior of GO film when outer GO was reduced to rGO and became hydrophobic.
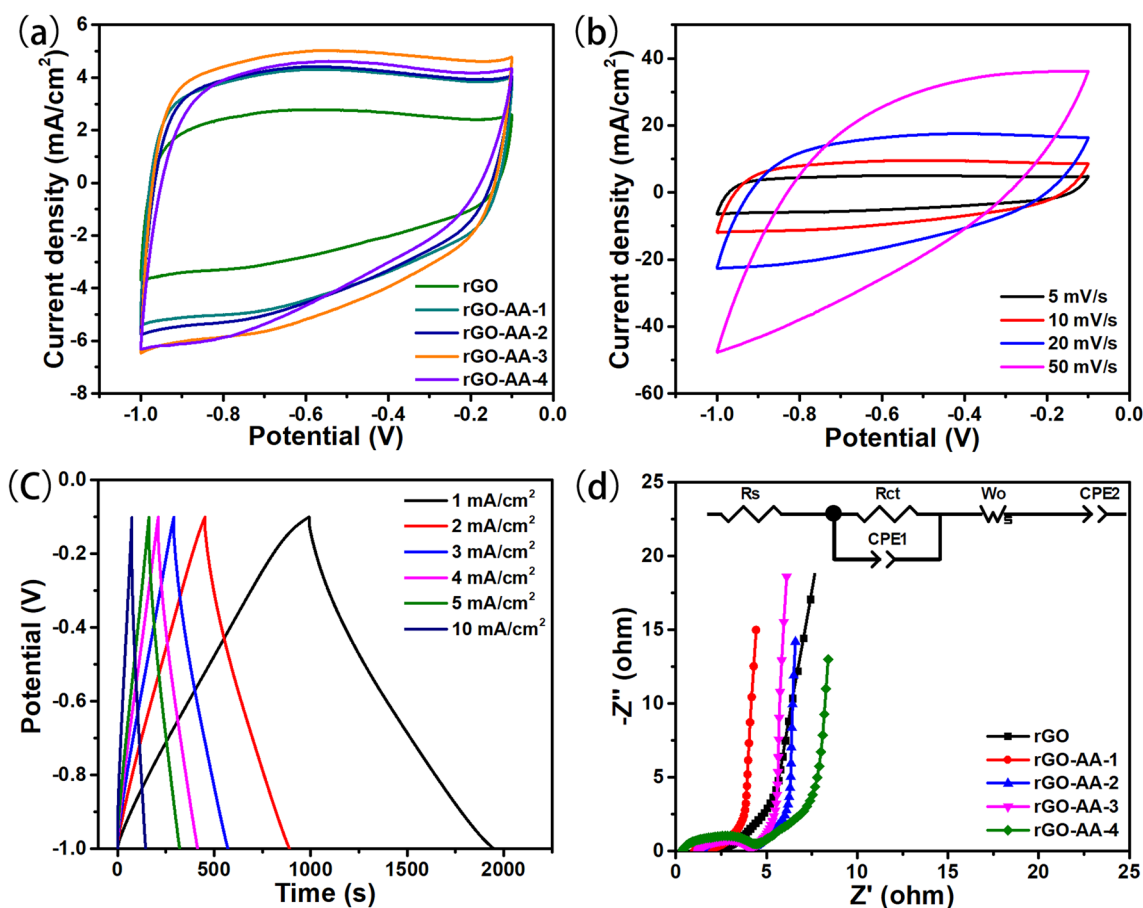
Fig. 1 **a** CV curves of rGO and rGO-AA-1~4 at scan rate of 5 mV/s, **b** CV curve of rGO-AA-3 at scan rate of 5, 10, 20, 50 mV/s, respectively, **c** GCD curves of rGO-AA-3 at current density of 1, 2, 3, 4, 5, and 10 mA/cm^2, respectively, **d** EIS spectrum of rGO and rGO-AA-1~4

Cai *et al. Collagen and Leather*   (2024) 6:9

Page 6 of 14

CV curves of rGO, rGO-AA-1, rGO-AA-2, rGO-AA-3, and rGO-AA-4 at a scanning rate of 5 mV/s are shown in Fig. 1a. When concentration of ascorbic acid were 0, 7.78, 15.56, 23.34, and 38.9 mg/mL, areal specific capacitance of rGO-AA were 967, 1524, 1555, 1786, and 1598 mF/cm^2, respectively. As concentration of ascorbic acid increased, specific capacitance of rGO-AA first increased and then decreased. The ascorbic acid remaining in the GO film can directly reduce internal GO during reduction process, thus increasing its specific capacitance. In addition, the ascorbic acid was oxidized to dehydroascorbic acid, which can be further converted into oxalic acid and gulosuronic acid [20]. The reduced graphene still had some oxygen-containing functional groups, while oxalic acid or gulosuronic acid could form hydrogen bonds with remaining oxygen-containing functional groups on the surface of rGO. This interaction could disrupt π–π stacking between rGO layers and prevent restacking. When concentration of ascorbic acid increases to 38.9 mg/mL, too much residual ascorbic acid led to a harm in conductivity and ion migration rate, resulting in decrease of specific capacitance.

Specific capacitance of rGO-AA-3 at different scanning rates is shown in Fig. 1b. At scanning rate of 5, 10, 20, and 50 mV/s, specific capacitance was 1786, 1646, 1438, and 1020 mF/cm^2, respectively, indicating a capacitance retention rate of 57.1%. Specific capacitance of rGO-AA-3 at different current densities is shown in Fig. 1c. At current density of 1, 2, 3, 4, 5, and 10 A/cm^2, specific capacitance is 1063, 973, 937, 907, 883, and 789 mF/cm^2, respectively, revealing a capacitance retention rate of 74.2%.

EIS spectra of rGO and rGO-AA are shown in Fig. 1d. The impedance spectrum was divided into three regions: high-frequency region in semi-circular, 45° linear intermediate-frequency region and vertical linear low-frequency region [21, 22]. The fitted CPE$_2$ increased first and then decreased (Table 3), and CPE$_2$ value of rGO-AA-3 is the maximum, which is consistent with variation of specific capacitance calculated through CV curves. The curve in the high-frequency region showed a semi-circular impedance response, which was an equivalent circuit feature of parallel capacitance and resistance [23]. Intercept between the high-frequency region and impedance real axis reflected the magnitude of electrolyte resistance (R$_S$) value, while intercept between the intermediate frequency region and impedance real axis reflected the overall resistance (R$_S$ + 1/2 R$_{CT}$) of electrode electrolyte system [24]. Among them, R$_{CT}$ was charge transfer resistance. Due to reduction of GO inside film by ascorbic acid, R$_{CT}$ of rGO-AA-1 decreased from 2.31 to 0.57 Ω/cm^2 compared to rGO. However, with increasing attachment of ascorbic acid to graphene sheets, their conductivity was reduced, leading to increase in R$_{CT}$. The mid frequency region was Warburg impedance region, which was related to diffusion and permeation of electrolyte on electrode surface [25]. When ascorbic acid reached 38.9 mg/mL, Wo-R of rGO-AA-4 significantly increased to 2.70 Ω/cm^2, indicating an increase in electrolyte transport resistance for blockage of ion transport channels by ascorbic acid.

3.2 Characterization of XCS and aXCS

In order to cut down the interlayer contact resistance of rGO film, XCS and aXCS were prepared. In hydrothermal reaction, xylan underwent hydrolysis, dehydration, polymerization and aromatization to generate carbon sphere [26]. By changing the solvent for dissolving xylan, concentration of xylan, and time of hydrothermal carbonization, xylan derived carbon spheres (XCS-1~6) were prepared and their SEM images are shown in Fig. 2. When 2% NaOH was used as solvent, a yellow viscous solution which was slightly turbid formed with addition of xylan, indicating a small part of xylan was still not completely dissolved. The prepared XCS-1 had a spherical prototype, but its morphology and size were uneven. After changing the solvent to NaOH/urea, xylan dissolved and formed a clear bright yellow solution. Size of XCS-2 obtained by hydrothermal carbonization was 0.2–2 μm, but surface of most carbon sphere was rough due to insufficient carbonization time. Extending the hydrothermal carbonization time to 24 h, XCS-3~6 was prepared, as shown in Fig. 2c, d.

When concentration of xylan was below 0.05 mg/mL (XCS-3 & XCS-4), due to the low concentration of xylan, carbon nuclei generated in solution was in low quantity and was generated throughout entire reaction process. The carbon nuclei initial formed by polymerization tended to grow into micrometer sized carbon spheres, resulting in different sizes of carbon spheres. Hence, XCS-3 & XCS-4 contained carbon spheres up to 5 μm and around 100 nm. When concentration of xylan increased to 0.05 mg/mL, sufficient carbon nuclei was generated in the initial stage of reaction, making it easier for decomposition products of xylan to polymerize

Table 3 Summarized equivalent circuit parameters from fitted Nyquist plot

|	R$_S$ (Ω)	R$_{CT}$ (Ω/cm^2)	W$_O$-R (Ω/cm^2)	CPE$_2$ (mF/cm^2)
rGO	1.74	2.31	1.88	460
rGO-AA-1	0.99	0.57	1.89	747
rGO-AA-2	1.33	2.04	1.55	764
rGO-AA-3	1.17	2.95	1.82	846
rGO-AA-4	0.27	2.67	2.70	794
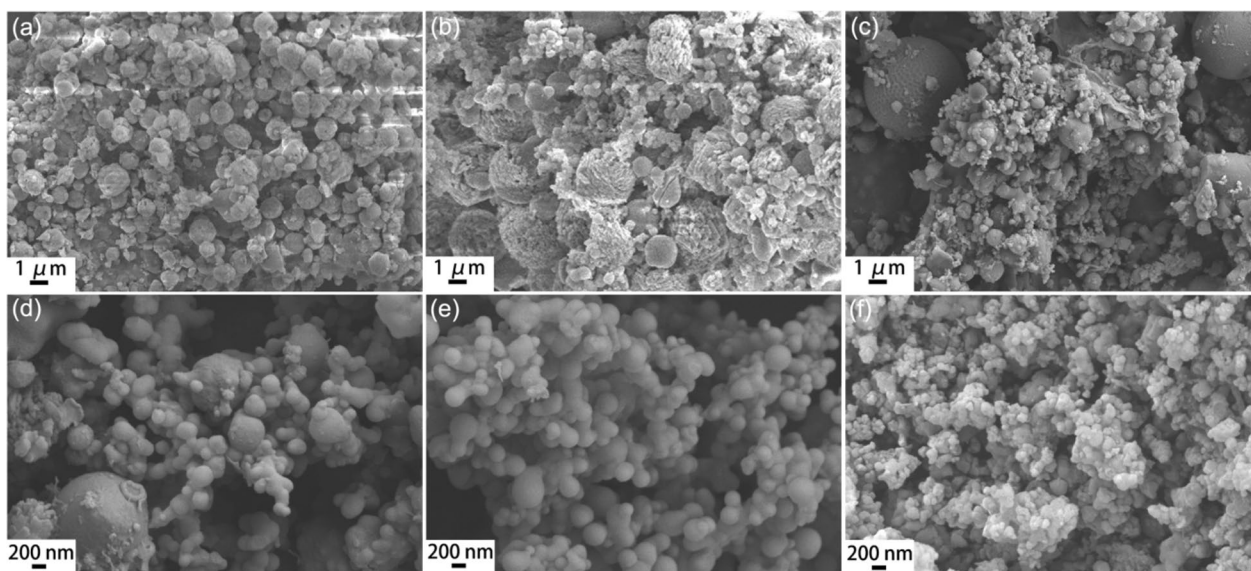
Fig. 2 SEM images of **a** XCS-1, **b** XCS-2, **c** XCS-3, **d** XCS-4, **e** XCS-5, **f** XCS-6

on surface of carbon nuclei. Meanwhile, formation of new carbon nuclei was inhibited, resulting in carbon spheres with smooth surface and uniform size around 150–200 nm. However, when the concentration of xylan increased to 0.1 g/mL, excessive content of xylan led to a rapid reaction rate and difficulty in forming carbon spheres with uniform size and spherical morphology. Therefore, carbon spheres were prepared by 0.05 g/mL xylan in NaOH/urea aqueous solution at 240 °C for 24 h.

Carbon materials for electrochemical capacitors requires good conductivity, high specific surface area, excellent corrosion resistance, high thermal stability, and electrically active substances [27]. However, the temperature of hydrothermal carbonization was lower, resulting in incomplete carbonization and poor conductivity of the prepared XCS-5. Specific capacitance of XCS-5 was very small, and when it was added to graphene, specific capacitance of this composite changed very little. Even, with the increasing dosage of XCS-5, specific capacitance decreased. Therefore, it was necessary to activate and carbonize the prepared carbon spheres at a higher temperature.

After immersing in KOH solution for 12 h, XCS-5 was centrifugated and dried in oven for 24 h, followed by high-temperature active carbonization in a tube furnace. Effects of KOH concentration, reaction temperature, and reaction time on the specific capacitance of aXCS were investigated (Fig. 3a). As concentration of KOH increased from 0.05 to 0.2 M, the specific capacitance increased from 52 to 270 F/g, indicating that high-temperature

activation of KOH successfully improved specific capacitance of carbon spheres through increasing conductivity of carbon spheres and surface pores. When concentration of KOH continued to increase to 0.25 M, the excessive reaction between KOH and carbon spheres severely disrupted structure of carbon spheres, reduced orderliness of graphite crystals and to some extent reduced conductivity [28], resulting in a decrease in specific capacitance to 178 F/g. As shown in Fig. 3b, specific capacitance of activated carbon spheres prepared under temperature of 700, 800, and 900 °C were 80, 270, and 112 F/g, respectively. 700 °C is relatively low and carbon spheres cannot be fully carbonized. In contrast, 900 °C is too high, the carbon spheres melt and specific capacitance decreased. CV curves of aXCS prepared at different reaction times are shown in Fig. 3c. Their specific capacitance activated at 0.5, 1, and 2 h were 108, 270, and 60 F/g, respectively. Therefore, the optimized condition for activating carbon spheres was 800 °C, 0.2 M KOH, and 1 h. CV curves of aXCS-2 prepared under this condition at different scanning rates are shown in Fig. 3d. Its specific capacitance measured at a scanning speed of 500 mV/s still maintained 70%, indicating good rate performance. The specific surface area of XCS-5 and aXCS-2 were investigated by BET and shown in Additional file 1: Table S1. The surface area of XCS-5 is 5.63 m^2/g with pore size of 127.57 Å. After active carbonization by KOH in 800 °C, surface area of aXCS-2 increases to 10.48 m^2/g and pore size decreases to 82.39 Å, indicating the etching of KOH on carbon sphere.
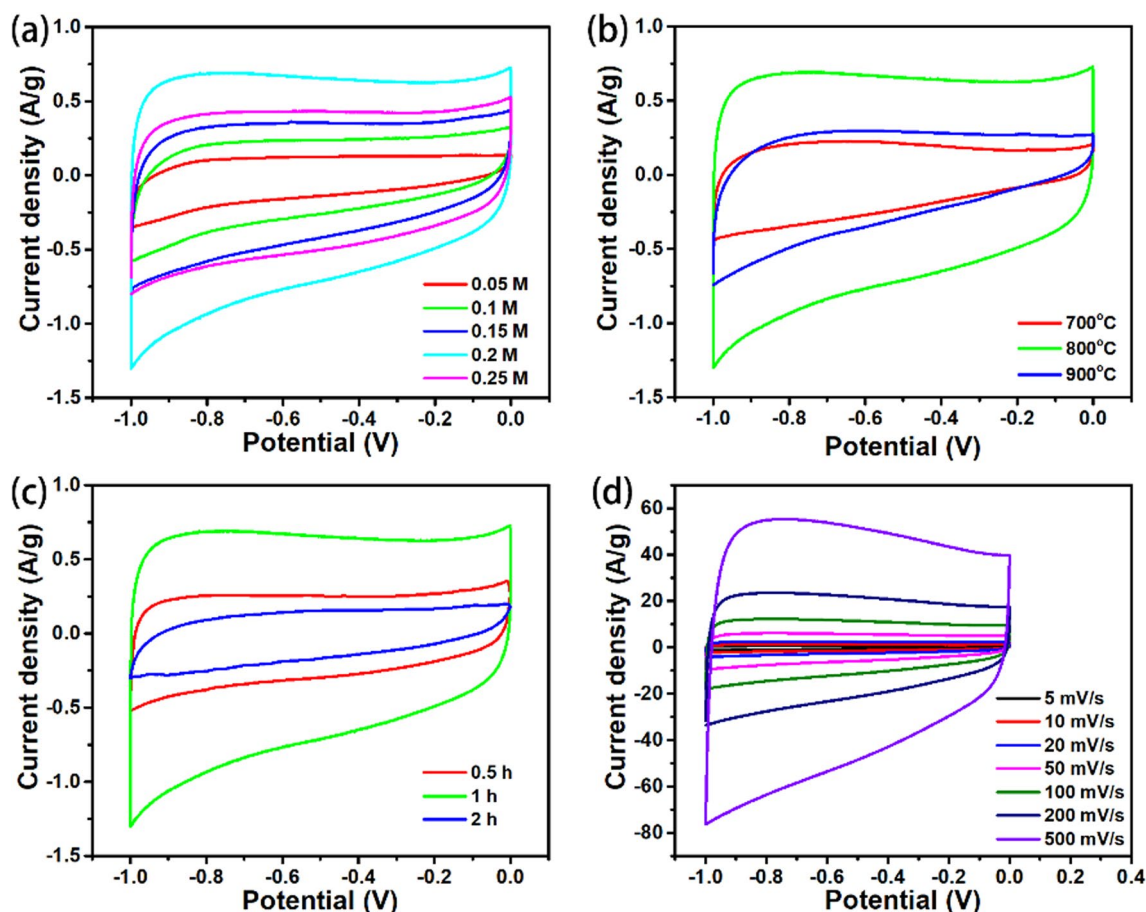
Fig. 3 **a** CV curves of aXCS-2 and aXCS-4~7 under scan rate of 5 mV/s, **b** CV curves of aXCS-1~3 under scan rate of 5 mV/s, **c** CV curves of aXCS-2, 8, 9 under scan rate of 5 mV/s, **d** CV curves of aXCS-2 under different scan rate

3.3 Electrochemical performance of aXCS/rGO composite film

After uniformly dispersing in water by ultrasound, aXCS suspension was added to GO solution under stirring, followed by filtration to form a film. Then, the film was reduced to prepare aXCS/rGO composite film with loading capacity of 3.77 mg/cm^2 GO. Their cyclic voltametric curve is shown in Fig. 4a. Meanwhile, calculated area specific capacitance and mass specific capacitance are shown in Table 4.

As amount of aXCS increased, specific capacitance of aXCS/rGO composite film gradually increased from 967 to 1878 mF/cm^2. This is because the addition of electrochemically active carbon spheres enhanced the specific capacitance of composite film which was proportionally with addition dosage. Its mass specific capacitance had a maximum value of 308 F/g at 20% aXCS addition, while specific capacitance of aXCS-2 and rGO were 270 F/g and 240 F/g, respectively. Carbon spheres served as spacer between graphene layers, providing charge transfer channels between graphene layers and reducing resistance. Therefore, mass specific capacitance of aXCS$_{0.2}$/rGO significantly improved compared with aXCS-2 and rGO. When content of aXCS increased to 40%, the excessive aXCS blocked diffusion channel of electrolyte ions, resulting in a decrease in mass specific capacitance. CV curves and GCD curves of aXCS$_{0.2}$/rGO at different scanning rates are shown in Fig. 4b, c. Area specific capacitance at 5, 10, 20, and 50 mV/s scanning rates were 1421, 1309, 1162, and 908 mF/cm^2, respectively, revealing a capacitance retention rate of 63.9%. GCD was a symmetrical straight line. At current densities of 1, 2, 5, and 10 mA/cm^2, the area specific capacitance were 773, 722, 656, and 588 mF/cm^2, respectively. The capacitance retention rate was 76.1%, indicating good rate performance.
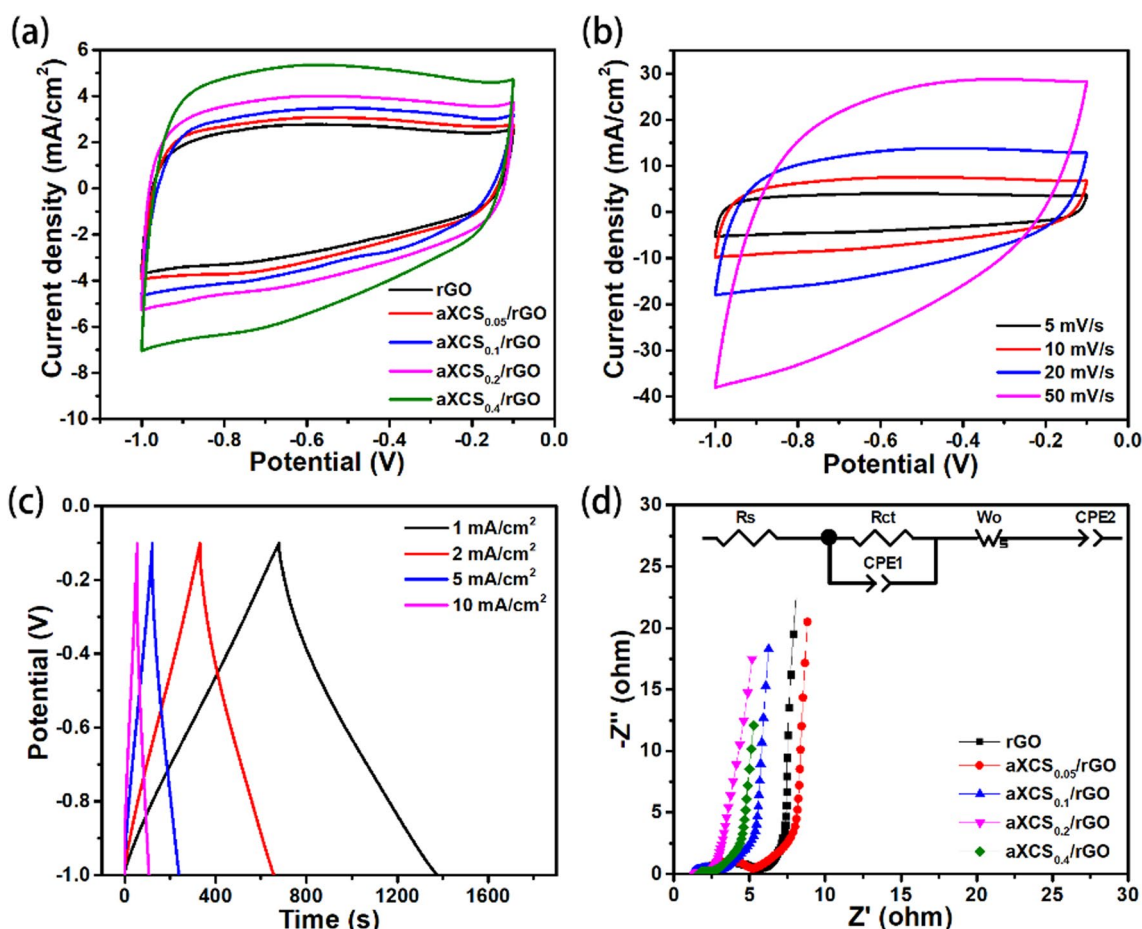
Fig. 4 a CV curves of rGO and aXCS$_{0.05-0.2}$/rGO at scan rate of 5 mV/s, **b** CV curves of aXCS$_{0.2}$/rGO at scan rate of 5, 10, 20, and 50 mV/s, **c** GCD curves of aXCS$_{0.2}$/rGO at current density of 1, 2, 5, 10 mA/cm^2, **d** EIS spectrum of rGO and aXCS$_{0.05-0.2}$/rGO

Table 4 Areal capacitance and specific capacitance of aXCS/rGO films

	rGO	aXCS$_{0.05}$/rGO	aXCS$_{0.1}$/rGO	aXCS$_{0.2}$/rGO	aXCS$_{0.4}$/rGO
Dosage of aXCS (%)	0	5	10	20	40
Areal capacitance (mF/cm^2)	967	1083	1222	1421	1878
Specific capacitance (F/g)	240	214	235	308	222

In order to investigate transfer characteristics of charges and ions on surface of aXCS/rGO film, their Nyquist curves and SEM images were measured (Figs. 4d and 5). The Nyquist curve could be fitted according to equivalent circuit shown in the inset of Fig. 4d, and the fitted parameters were shown in Table 5.

Under directional arrangement of water flow during filtration, graphene exhibits a regular layered structure (Fig. 5a, b). Electron transfer in layer was fast but became slow between layers, leading to high R_{CT}. Meanwhile interlayer space acted as pathway for infiltration of electrolyte ion. With addition of aXCS, there were carbon

Cai *et al. Collagen and Leather*   (2024) 6:9

Page 10 of 14
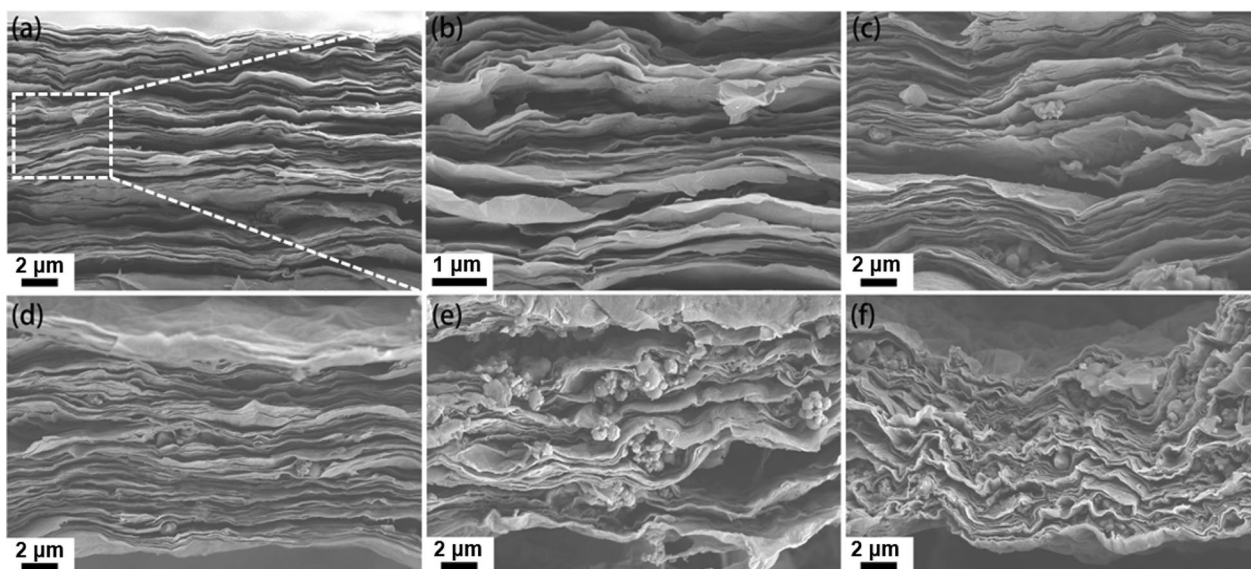
Fig. 5 SEM images of the cross section: **a** rGO, **b** magnified images of a, **c** aXCS$_{0.05}$/rGO, **d** aXCS$_{0.1}$/rGO, **e** aXCS$_{0.2}$/rGO, **f** aXCS$_{0.4}$/rGO

Table 5 Summarized equivalent circuit parameters from fitted Nyquist plot

	R$_S$ (Ω)	R$_{CT}$ (Ω/cm²)	Wo-R (Ω/cm²)	CPE$_2$ (mF/cm²)
rGO	1.74	2.31	1.88	460
aXCS$_{0.05}$/rGO	1.74	2.33	2.17	503
aXCS$_{0.1}$/rGO	1.18	1.12	2.07	577
aXCS$_{0.2}$/rGO	1.21	0.84	2.48	676
aXCS$_{0.4}$/rGO	1.60	0.69	6.01	721

spheres implanted in the interlayer space (Fig. 5c–f). The unsatisfactory dispersion performance may due to self-assembly of GO and aXCS under pressure induced by vacuum filtration. Although the GO shows a lateral dimension in micrometer, its thickness is several nanometers. Hence, the nanosheet of GO is not stiff enough to support solid aXCS with diameter of 150–200 nm. When aXCS are decorated on GO nanosheet under pressure, the GO nanosheet may form concavity which agglomerates neighboring carbon spheres and leads to unsatisfactory dispersion. These aXCSs with high conductivity connected layer of graphene, which provided channels for charge transfer and decreased contact resistance between layers. Therefore, R$_{CT}$ value continued to decrease due to efficient charge transfer between graphene layers bridged by aXCS. In the meantime, addition of aXCS occupied the interlayer space and made the composite film become

dense, which blocked transmission channel of electrolyte between graphene layers and hindered transmission of electrolyte ions. Thus, Warburg resistance and frequency domain range became larger with increase of aXCS dosage. And response of virtual impedance $-Z''$ in low frequency region was nearly perpendicular, indicating that electrolyte ions had a fast charge transfer with small diffusion transfer restrictions.

The electrolyte and electrode resistance of aXCS$_{0.2}$/rGO were as small as 1.21 Ω and 0.84 Ω, respectively. The static specific capacitance derived at low frequency was 676 mF/cm². Compared with rGO, the increase of Warburg resistance caused by addition of carbon spheres was not significant, while the charge transfer resistance was greatly reduced, resulting in a lower mass specific capacitance.

3.4 Electrochemical performance of aXCS/rGO-AA composite film

Adding 20% aXCS and 23.34 mg/mL ascorbic acid to GO solution, aXCS/rGO-AA film was obtained by filtering and reducing. Its CV curve is shown in Fig. 6a. At scanning rate of 5, 10, 20, and 50 mV/s, the specific capacitance were 1849, 1661, 1349, and 815 mF/cm², respectively, indicating a capacitance retention rate of 44.1%. The GCD curve and specific capacitance of aXCS/rGO-AA are shown in Fig. 6b, c. When current density were 1, 2, 3, 4, 5, and 10 mA/cm², the specific capacitance

Cai *et al. Collagen and Leather*   (2024) 6:9

Page 11 of 14
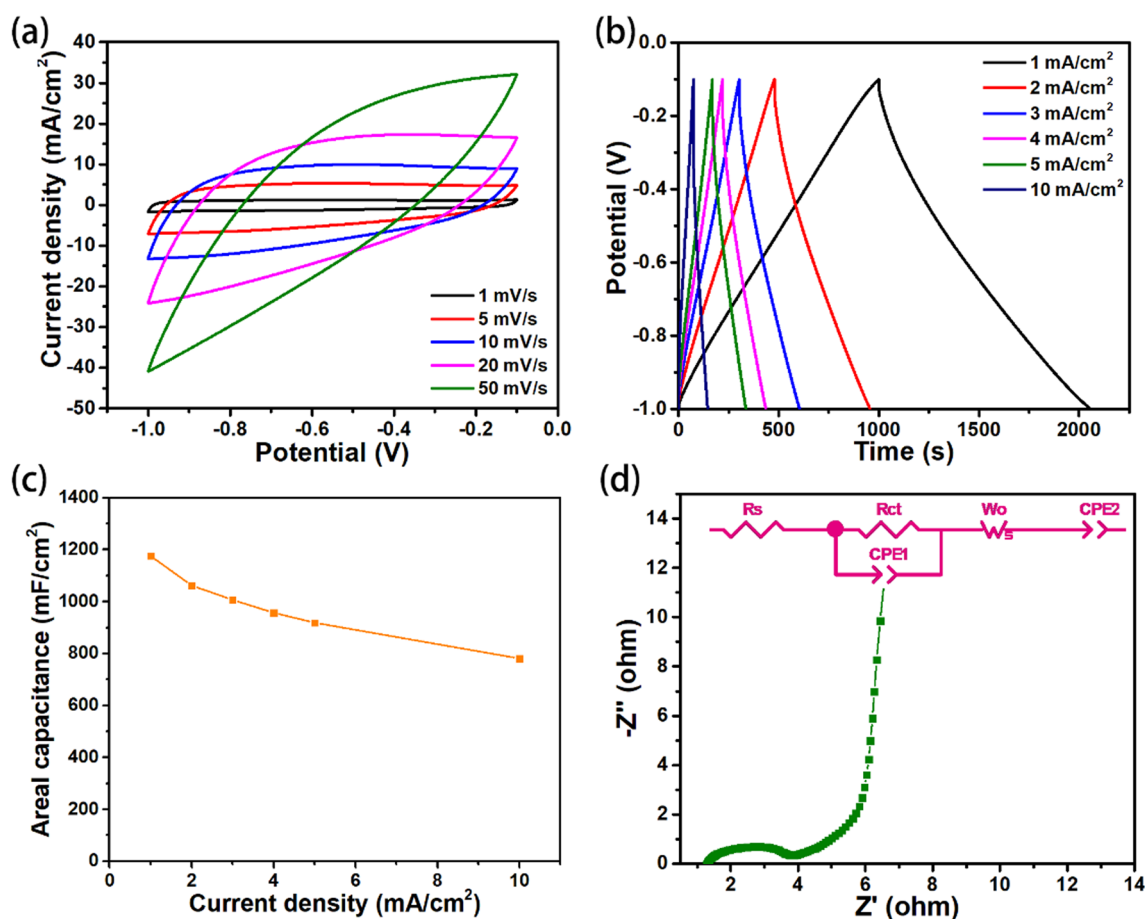
Fig. 6 **a** CV curves of aXCS/rGO-AA, **b** GCD curves of aXCS/rGO-AA, **c** Ragone plot of aXCS/rGO-AA, **d** Nyquist curve of aXCS/rGO-AA

were 1176, 1062, 1007, 957, 919, and 781 mF/cm^2, respectively, and capacitance retention rate was 66.4%. Nyquist curve of aXCS/rGO-AA is shown in Fig. 6d, and can be fitted according to equivalent circuit. The fitted parameters R_S, R_{CT}, Wo-R, and CPE$_2$ were 1.23 Ω, 1.67 Ω/cm^2, 1.76 Ω/cm^2, and 872 mF/cm^2, respectively.

In order to characterize electrochemical performance of aXCS/rGO-AA under practical conditions, CV curves and GCD of two electrode system were tested (Fig. 7a). Its specific capacitance was 1282 mF/cm^2 at scanning rate of 5 mV/s. Area specific capacitance at different current densities is shown in Fig. 7b. The specific capacitance was 755 mF/cm^2 at the current density of 1 mA/cm^2. When current density was 10 mA/cm^2, capacitance retention rate was 55.6%. The relationship between power density and energy density is shown in Fig. 7d. When current density increased from 0.1 to 10 mA/cm^2, power density increased from 22.5 to 2250 mW/cm^2,

and energy density decreased from 0.0252 to 0.01188 Wh/cm^2.

Gradient discharging test for supercapacitor was investigated, shown in Fig. 8a. Figure 8a shows the discharge of aXCS/rGO-AA under varied current densities from 1 mA/cm^2 to 10 mA/cm^2 in two-electrode system, and the areal capacitances keep stable in 10 cycles at each step. After 6-step increase of current, the current density and areal capacitance of aXCS/rGO-AA return back to 1 mA/cm^2 and 1662 mF/cm^2, respectively, evidencing the impressive stability. Cyclic stability of aXCS/rGO-AA was determined by 10,000 CV scans (Fig. 8b), with a scanning rate of 50 mV/s. After 10,000 scans, the capacitance increased to 108.7%, indicating good stability performance. The fluctuate of capacity in 10,000 cycles of CV may due to the redox of ascorbic acid and permeation of KOH to interlayer. There are ascorbic acid and its derivative remained in aXCS/rGO-AA. In the cycle of CV scan, the redox of
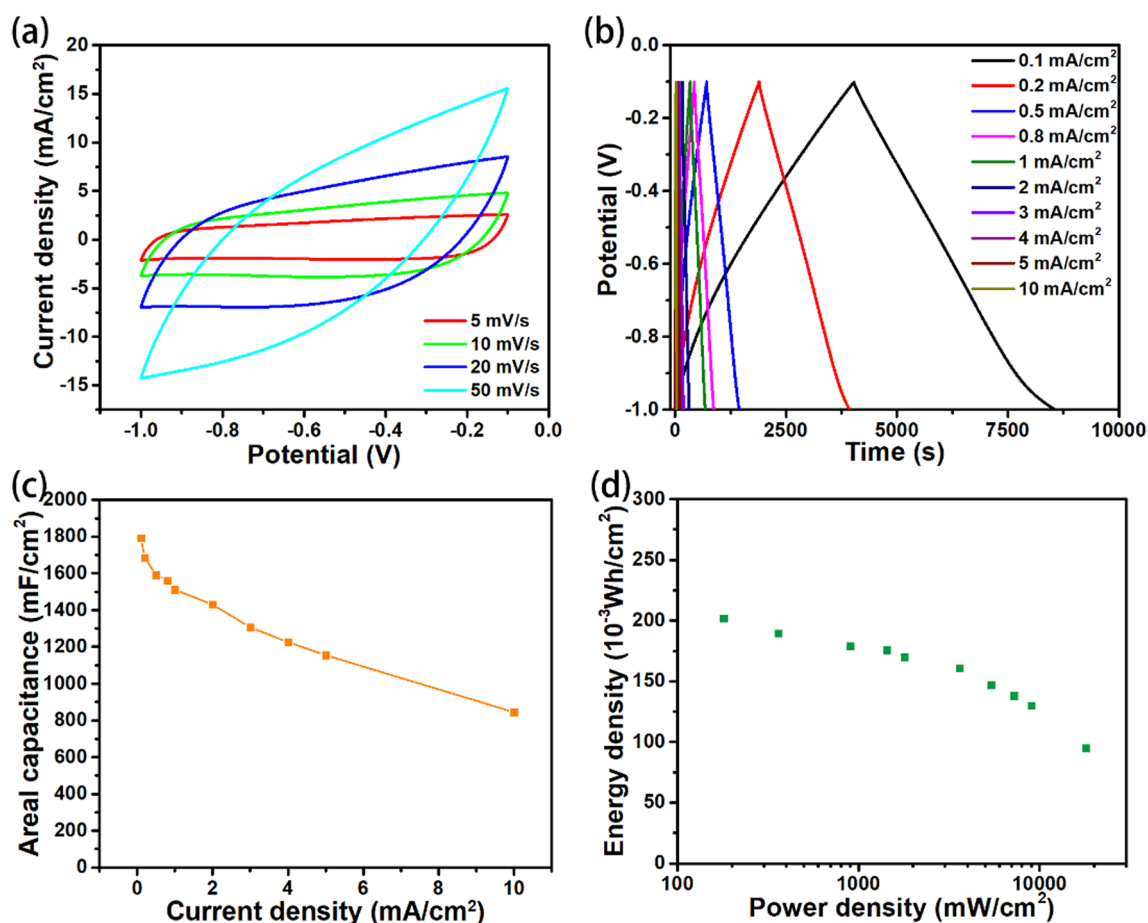
Fig. 7 Two electrode system: **a** CV curves of aXCS/rGO-AA, **b** GCD curves of aXCS/rGO-AA, **c** Areal capacitance of aXCS/rGO-AA under various current density, **d** Ragone plot of aXCS/rGO-AA

ascorbic acid provides a part of pseudo-capacitance, which will permanent loss after the complete consume. And the release of CO_2, the final product of redox of ascorbic acid, will also impact the double layer system of aXCS/rGO-AA and cause instability of capacitance. Furthermore, with the circulating of CV, more and more KOH will permeation to the interlayer of aXCS/rGO-AA, which provides more charge to storage for double-layer capacitance. Therefore, when ascorbic acid in aXCS/rGO-AA is exhausted at 7000 cycles, the fluctuate terminates and capacity increases steady. The SEM images of aXCS/rGO-AA before and after scan were investigated, as shown in Fig. 8c, d. The surface of aXCS/rGO-AA is crumpled like undulating hills as the graphene is covered on spherical aXCS. After scan, its surface becomes wizened due to the repeated adsorption–desorption of electrolyte ions.

4 Conclusions

The utilization of carbon sphere which derived from renewable xylan in fabrication of graphene-based supercapacitor largely enhances its performance. The intercalation of carbon sphere as spacer and connector to graphene sheets avoids restacking of graphene sheets and decreases interlayer contact resistance. Meanwhile, the *in-situ* reduction of GO by built-in ascorbic acid boosts charge transfer. As a result, aXCS/rGO-AA composite film shows an increased specific capacitance of 755 mF/cm^2 (current density 1 mA/cm^2) in the double electrode system, power density of 22.5–2250 mW/cm^2, and energy density of 11.88–25.2 mWh/cm^2, which will provide a new method for the fabrication of outstanding electrode.

Cai *et al. Collagen and Leather*   (2024) 6:9

Page 13 of 14
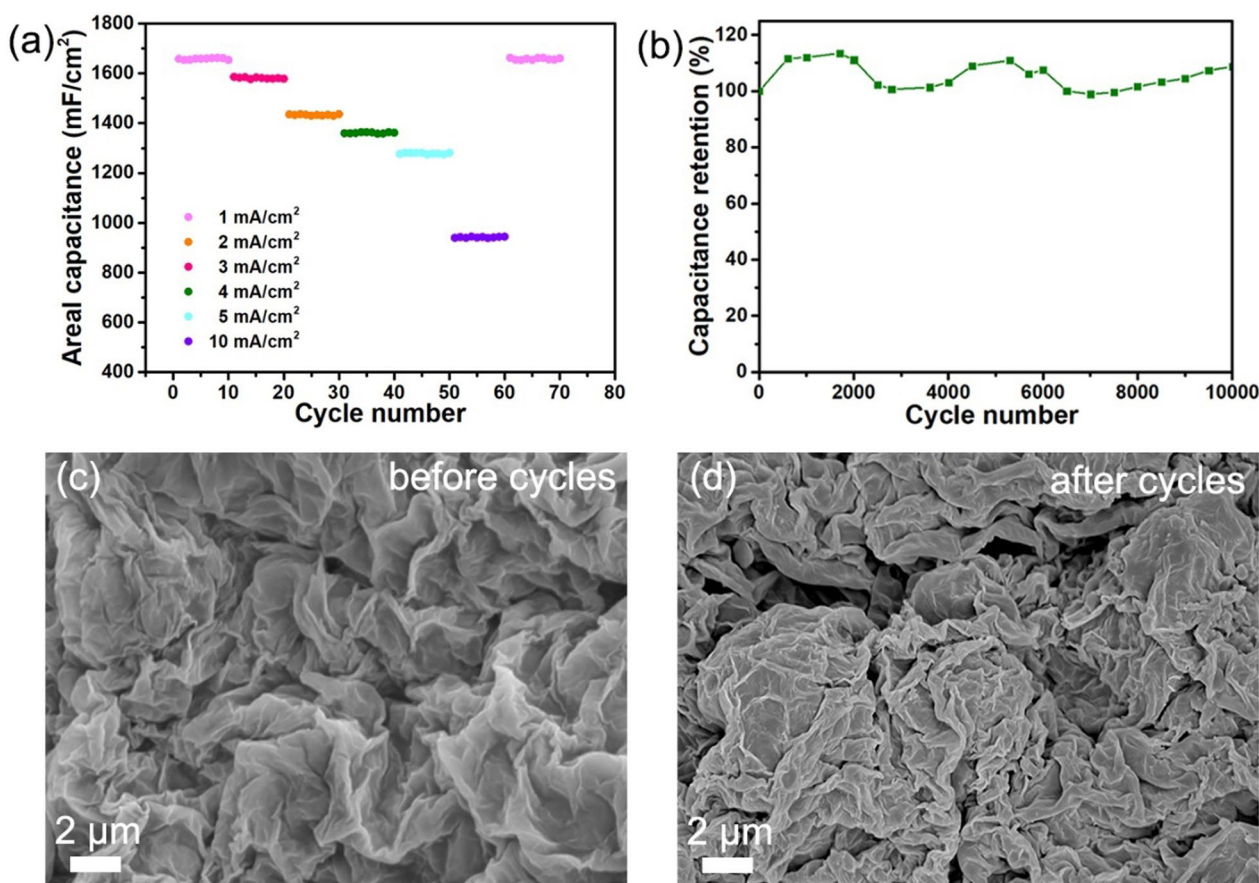
Fig. 8 **a** Discharging and resultant areal capacitance of aXCS/rGO-AA, **b** Capacity retention during 10,000 cycles of CV (scan rate 50 mV/s), **c** SEM images of aXCS/rGO-AA before cycles and **d** after cycles

Supplementary Information

The online version contains supplementary material available at https://doi.org/10.1186/s42825-024-00154-w.

> **Additional file 1**. Electrochemical performance of rGO film, images of aXCS dispersion in water, and textural properties of carbon sphere before and after activation.

Author contributions

JC: Investigation, writing—original draft and funding acquisition; YL: Project administration; RQ: Resources and Funding acquisition; GL: Validation; XW: Supervision and writing—review & editing.

Availability of data and materials

Data will be made available on request.

Declarations

Competing interests

The authors declare that they have no known competing financial interests or personal relationships that could have appeared to influence the work reported in this paper.

Author details

[1]State Key Laboratory of Pulp and Paper Engineering, South China University of Technology, Guangzhou 510640, China. [2]School of Food Science and Engineering, Ocean University of China, Qingdao 266100, China. [3]Shandong Yinuokang Pharmaceutical Co., Ltd, Dongying 257000, China.

Cai *et al. Collagen and Leather*   (2024) 6:9

Page 14 of 14

References

1. Goda ES, Lee S, Sohail M, Yoon KR. Prussian blue and its analogues as advanced supercapacitor electrodes. J Energy Chem. 2020;50:206–29. https://doi.org/10.1016/j.jechem.2020.03.031.
2. Ajdari FB, Kowsari E, Shahrak MN, Ehsani A, Kiaei Z, Torkzaban H, Ershadi M, Eshkalak SK, Haddadi-Asl V, Chinnappan A, Ramakrishna S. A review on the field patents and recent developments over the application of metal organic frameworks (MOFs) in supercapacitors. Coord Chem Rev. 2020;422:213441. https://doi.org/10.1016/j.ccr.2020.213441.
3. Gu TH, Kwon NH, Lee KG, Jin XY, Hwang SJ. 2D inorganic nanosheets as versatile building blocks for hybrid electrode materials for supercapacitor. Coord Chem Rev. 2020;421:213439. https://doi.org/10.1016/j.ccr.2020.213439.
4. Zhang C, Nicolosi V. Graphene and MXene-based transparent conductive electrodes and supercapacitors. Energy Stor Mater. 2019;16:102–25. https://doi.org/10.1016/j.ensm.2018.05.003.
5. Li B, Yu M, Li Z, Yu C, Wang H, Li Q. Constructing flexible all-solid-state supercapacitors from 3D nanosheets active bricks via 3D manufacturing technology: a perspective review. Adv Funct Mater. 2022;32:2201166. https://doi.org/10.1002/adfm.202201166.
6. Chen H, Müller MB, Gilmore KJ, Wallace GG, Li D. Mechanically strong, electrically conductive, and biocompatible graphene paper. Adv Mater. 2008;20:3557–61. https://doi.org/10.1002/adma.200800757.
7. Yang ZG, Liu NN, Dong S, Tian FS, Gao YP, Hou ZQ. Supercapacitors based on free-standing reduced graphene oxides/carbon nanotubes hybrid films. SN Appl Sci. 2018;1:47. https://doi.org/10.1007/s42452-018-0059-y.
8. Luo J, Kim J, Huang J. Material processing of chemically modified graphene: some challenges and solutions. Acc Chem Res. 2013;46:2225–34. https://doi.org/10.1021/ar300180n.
9. Xiong ZY, Cao Y, Jiang WJ, Zu LH, Liang QH, Li D. Shearing induced ordered structures in two-dimensional nanomaterials-based electrodes for boosted pseudocapacitive kinetics. Energy Stor Mater. 2022;53:444–52. https://doi.org/10.1016/j.ensm.2022.09.026.
10. Yu Y, Xu A, Zhang Y, Li W, Qin Y. Evaporation-induced hydrated graphene/polyaniline/carbon cloth integration towards high mass loading supercapacitor electrodes. Chem Eng J. 2022;445:136727. https://doi.org/10.1016/j.cej.2022.136727.
11. Ye W, Cai J, Yu F, Li X, Wang X. Nitrogen-doped bagasse carbon spheres/graphene composite for high-performance supercapacitors. Biomass Bioenergy. 2021;145:105949. https://doi.org/10.1016/j.biombioe.2020.105949.
12. Guo J, Xu J, Xiao X, Dai L, Zhang C, Huo K. Integrating energy-environmental functions into multifaceted lignocellulose valorization: high-performance supercapacitors and antibiotic decomposition. Green Chem. 2022;24:8827–39. https://doi.org/10.1039/d2gc03100k.
13. Song E, Chae KB, Gu MG, Lee SH, Kim SK. Monodisperse starburst carbon spheres-intercalated graphene nanohybrid papers for supercapacitor electrodes. J Electroanal Chem. 2019;853:113533. https://doi.org/10.1016/j.jelechem.2019.113533.
14. Puchart V, Biely P. Microbial xylanolytic carbohydrate esterases. Essays Biochem. 2023;67:479–91. https://doi.org/10.1042/EBC20220129.
15. Cai JH, Han GD, Ren JL, Liu CF, Wang JL, Wang XY. Single-layered graphene quantum dots with self-passivated layer from xylan for visual detection of trace chromium(VI). Chem Eng J. 2022;435:131833. https://doi.org/10.1016/j.cej.2021.131833.
16. Falco C, Sieben JM, Brun N, Sevilla M, van der Mauelen T, Morallon E, Cazorla-Amoros D, Titirici MM. Hydrothermal carbons from hemicellulose-derived aqueous hydrolysis products as electrode materials for supercapacitors. Chemsuschem. 2013;6:374–82. https://doi.org/10.1002/cssc.201200817.
17. Zhao J, Pei S, Ren W, Gao L, Cheng HM. Efficient preparation of large-area graphene oxide sheets for transparent conductive films. ACS Nano. 2010;4:5245–52. https://doi.org/10.1021/nn1015506.
18. Ma R, Cao L, Zhuo J, Lu J, Chen J, Huang J, Yang G, Yi F. Designed redox-electrolyte strategy boosted with electrode engineering for high-performance $Ti_3C_2T_x$ MXene-based supercapacitors. Adv Energy Mater. 2023. https://doi.org/10.1002/aenm.202301219.
19. Jung YM, Choi JH, Kim DW, Kang JK. 3D porous oxygen-doped and nitrogen-doped graphitic carbons derived from metal azolate frameworks as cathode and anode materials for high-performance dual-carbon sodium-ion hybrid capacitors. Adv Sci. 2023. https://doi.org/10.1002/advs.202301160.
20. Palomba M, Carotenuto G, Longo A. A brief review: The use of l-ascorbic acid as a green reducing agent of graphene oxide. Materials (Basel). 2022;15:6456. https://doi.org/10.3390/ma15186456.
21. William JJ, Babu IM, Muralidharan G. Nickel bismuth oxide as negative electrode for battery-type asymmetric supercapacitor. Chem Eng J. 2021;422:130058. https://doi.org/10.1016/j.cej.2021.130058.
22. Han J, Choi Y, Lee J, Pyo S, Jo S, Yoo J. UV curable ionogel for all-solid-state supercapacitor. Chem Eng J. 2021;416:129089. https://doi.org/10.1016/j.cej.2021.129089.
23. Xu T, Yang D, Zhang S, Zhao T, Zhang M, Yu ZZ. Antifreezing and stretchable all-gel-state supercapacitor with enhanced capacitances established by graphene/PEDOT-polyvinyl alcohol hydrogel fibers with dual networks. Carbon. 2021;171:201–10. https://doi.org/10.1016/j.carbon.2020.08.071.
24. Zhang Q, Li Y, Zhu J, Lan L, Li C, Mao J, Wang F, Zhang Z, Wang L. Ultra-low temperature flexible supercapacitor based on hierarchically structured pristine polypyrrole membranes. Chem Eng J. 2021;420:129712. https://doi.org/10.1016/j.cej.2021.129712.
25. Zhang G, Hu J, Nie Y, Zhao Y, Wang L, Li Y, Liu H, Tang L, Zhang X, Li D, Sun L, Duan H. Integrating flexible ultralight 3D Ni micromesh current collector with NiCo bimetallic hydroxide for smart hybrid supercapacitors. Adv Funct Mater. 2021;31:2100290. https://doi.org/10.1002/adfm.202100290.
26. Titirici MM, Antonietti M. Chemistry and materials options of sustainable carbon materials made by hydrothermal carbonization. Chem Soc Rev. 2010;39:103–16. https://doi.org/10.1039/b819318p.
27. Bose S, Kuila T, Mishra AK, Rajasekar R, Kim NH, Lee JH. Carbon-based nanostructured materials and their composites as supercapacitor electrodes. J Mater Chem. 2012;22:767–84. https://doi.org/10.1039/c1jm14468e.
28. Wang Y, Yang R, Li M, Zhao Z. Hydrothermal preparation of highly porous carbon spheres from hemp (*Cannabis sativa* L.) stem hemicellulose for use in energy-related applications. Ind Crop Prod. 2015;65:216–26. https://doi.org/10.1016/j.indcrop.2014.12.008.

Publisher's Note

Springer Nature remains neutral with regard to jurisdictional claims in published maps and institutional affiliations.